Cronfa - Swansea University Open Access Repository

_____

Cronfa URL for this paper:

_____

Paper:

_____

http://www.swansea.ac.uk/library/researchsupport/ris-support/

PAPER

Thermal decomposition of ammonium hexachloroosmate†

T. I. Asanova,*[a] I. Kantor,[bc] I. P. Asanov,[ad] S. V. Korenev[ad] and K. V. Yusenko[e]

Structural changes of $(NH_4)_2[OsCl_6]$ occurring during thermal decomposition in a reduction atmosphere have been studied *in situ* using combined energy-dispersive X-ray absorption spectroscopy (ED-XAFS) and powder X-ray diffraction (PXRD). According to PXRD, $(NH_4)_2[OsCl_6]$ transforms directly to metallic Os without the formation of any crystalline intermediates but through a plateau where no reactions occur. XANES and EXAFS data by means of Multivariate Curve Resolution (MCR) analysis show that thermal decomposition occurs with the formation of an amorphous intermediate $\{OsCl_4\}_x$ with a possible polymeric structure. Being revealed for the first time the intermediate was subjected to determine the local atomic structure around osmium. The thermal decomposition of hexachloroosmate is much more complex and occurs within a minimum two-step process, which has never been observed before.

1. Introduction

Ammonium hexachlorometalates $(NH_4)_2[MCl_6]$ (M = Pt, Pd, Ir, Os, Re) with a cubic crystal structure of the $Fm\bar{3}m$ space group have been well-known as complex compounds since 1817.[1,2] $(NH_4)_2[MCl_6]$ can be easily synthesized in water solutions and traditionally used as precursors for many industrial scale processes such as preparation of active pharmaceutical ingredients, heterogeneous electro-catalysts as well as various nanocomposite materials.[3–5] While the thermal reactivity of hexachlorometalates plays an important role in understanding their stability and transformations in the solid state, their thermal decomposition in the solid state was studied after the first thermal analysis techniques were developed.[2] Recent developments in precise *in situ* in-house and synchrotron-based techniques including time resolved X-ray diffraction and fast X-ray absorption spectroscopy where each data point can be collected within seconds[6,7] and even microseconds[8–10] make possible the re-evaluation of our knowledge about many classical reactions in solution and solid state.

Thermal decomposition of ammonium hexachlorometalates has been mainly investigated in an inert atmosphere. Previous TG (thermogravimetric) data collected in an inert atmosphere

for $(NH_4)_2[MCl_6]$ salts with Ir, Re and Os did not suggest the formation of any intermediates in the following stoichiometric reaction:[11]

$$3(NH_4)_2[MCl_6] \rightarrow 3M + 2N_2 + 16HCl + 2NH_4Cl \quad (1)$$
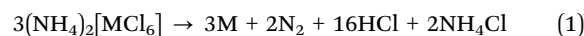
Thermal decomposition of Pt and Pd $(NH_4)_2[MCl_6]$ salts seems to be particularly complicated. *In situ* XAFS experiments with $(NH_4)_2[PdCl_6]$ at Cl K- and Pd/Rh L_3-edges[12] suggested the formation of several intermediates such as $Pd(NH_3)Cl_5$, *trans*-$Pd(NH_3)_2Cl_2$ or $(NH_4)_2[PdCl_4]$. A similar experiment with $(NH_4)_2[PtCl_6]$[13] revealed a fingerprint of *cis*-$Pt(NH_3)_2Cl_2$, however, by considering some other platinum amine complexes as intermediates. Direct evidence of *cis*-$Pt(NH_3)_2Cl_2$ formation has been recently obtained using microsecond time-resolved energy dispersive EXAFS[9] proving the two-step thermal reaction process:

$$(NH_4)_2[PtCl_6] \rightarrow cis\text{-}Pt(NH_3)_2Cl_2 \rightarrow Pt \quad (2)$$
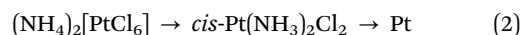
Such findings suggest that a visually simple reaction being investigated by more powerful techniques with more precision may open many unsolved problems and show a high level of complexity. The application of *in situ* techniques with ultra-fast time resolution may provide important information about the process including kinetic data.

In the present study we report *in situ* energy-dispersive XAFS and fast time-resolved PXRD investigation of the thermal decomposition process of ammonium hexachloroosmate, $(NH_4)_2[OsCl_6]$. Each of these methods is used for studying solid-state chemical reactions accompanied by structural and compositional transformations as well as a number of phases/species.[14–16] However, the combination of the methods has been shown to be more powerful because one provides changes in both short- and long-range atomic

[a] Nikolaev Institute of Inorganic Chemistry SB RAS, 3, Acad. Lavrentiev Ave., Novosibirsk, Russia. E-mail: nti@niic.nsc.ru

[b] European Synchrotron Radiation Facility, F-38043 Grenoble, France

[c] Technical University of Denmark, Department of Physics, Fysikvej 307, 2800 Kgs, Lyngby, Denmark

[d] Novosibirsk State University, Novosibirsk, 2 Pirogova Str, Novosibirsk, Russia

[e] College of Engineering, Swansea University, Bay Campus, Fabian Way, Swansea SA1 8EN, UK

order during chemical transformation.[17–20] Hydrogen has been applied as a reducing agent to initiate the following stoichiometric reaction:

$$(NH_4)_2[OsCl_6] + 2H_2 \rightarrow Os + 2NH_4Cl + 4HCl \quad (3)$$

2. Experimental

Polycrystalline $(NH_4)_2[OsCl_6]$ has been obtained from abcr GmbH & Co. KG (Germany).

An *in situ* XAFS experiment was performed on ID24 beamline at the European Synchrotron Radiation Facility. More information about the beamline layout can be found elsewhere.[21] For XAFS experiments, a mixture of polycrystalline $(NH_4)_2[OsCl_6]$ and BN (1:10 volume ratio) was pressed in a pellet. Os L_3-edge XAFS spectra were collected in the transmission mode upon heating (6 K min^{-1}) in a reducing atmosphere (2 vol% H_2/He). A FReLoN (Fast-Readout Low-Noise) high-frame-rate detector was used for fast continuous collection of X-ray absorption spectra.[22] In the used energy-dispersive XAFS scheme the full spectrum (I_{sample}) is recorded at once when the beam passes through the sample, with an exposure time of 0.2 s (200 accumulations of 1 ms each). Immediately after that, the sample was removed from the beam and the same spectrum of the upcoming beam (I_0) was recorded, with an exposure time of 0.1 s (200 accumulation of 0.5 ms). The resultant XAS spectrum was calculated as $-\ln(I_{sample}/I_0)$. The time lag between I_0 and I_{sample} recordings was approximately 2 s. A Pt foil was used as a reference for pixel-to-energy calibration. X-ray beam was re-focused vertically using a silicon mirror, so that the final X-ray spot size on the sample was 15(v) × 7(h) μm^2, FWHM. XAFS spectra were analysed using IFEFFIT software.[23,24]

Multivariate curve resolution-alternative least squares (MCR-ALS) analysis of XANES and EXAFS ($\chi(k)$) was performed for a selection of the contributions of the different species to the experimental spectra.[25,26] In the framework of the MRS-ALS method, the experimental data matrix D is represented as a bilinear model of the pure components

$$D = CS^T + E \quad (4)$$

The data matrix D encloses measured intensities in columns and measured samples (in our case, different temperatures) in rows. C is a matrix of concentrations showing contributions of the pure components to the measured spectra. S^T is a transpose of the matrix of the pure component spectra, and E is a matrix of residuals representing the unexplained variance of data. For the self-consistent analysis of the same samples using XANES and EXAFS methods, we used a multi-set analysis using the augmented row-wise data matrix. In this case, we analysed the following equation:

$$[D_{XANES}D_{EXAFS}] = [C^i][S^i_{XANES}S^i_{EXAFS}] + [E^i_{XANES}E^i_{EXAFS}] \quad (5)$$

Here, the data matrix D, the matrix of the component spectra S and the matrix of residuals E enclose two sub-blocks describing XANES and EXAFS, correspondingly. The number of components is determined based on the results of principal component analysis. The initial estimations were selected by recognizing that in the initial and final stages of the thermal process only the spectra of the complex salt or the metal are present, respectively. The preliminary estimations were obtained using XANES data only and consequently applied for the total simultaneous multi-set analysis of XANES and EXAFS data. In the analysis procedure, we used the non-negativity constraints for concentration and XANES intensities using the fnnls algorithm,[26] the unimodality constraint for concentration using the average option with 10% tolerance for all the species, and the condition of invariability of osmium with the total closure constant equal to 1 for all the components. The quality of fitting was estimated using the following parameters: the percentage of variance explained R^2 and lack of fit (%).[26] At the optimum, the lack of the fit of the experimental data matrix[25] was 3.8%, and the percentage of variance obtained was 99.86%. Details of the MRS-ALS analysis can be also found elsewhere.[27]

In situ PXRD experiments were performed at the Swiss-Norwegian Beam Lines (BM01A), ESRF. The sample for the PXRD experiment was placed in a 0.5 mm fused quartz mark tube (Hilgenberg GmbH, Germany) and heated in a 2 vol% H_2/He flow (0.1–0.5 ml min^{-1}) with a hot air stream from room temperature to 1000 K with a ramp rate of 10 K min^{-1}. Temperature has been calibrated using thermal expansion of the cell parameters for the silver powder as the external standard. The wavelength (λ = 0.68894 Å) and the sample-to-detector distance have been calibrated using a LaB_6 powder (NIST SRM 660c) as an external standard. Data were collected every 20 s (3 K per minute on the temperature scale) using a PILATUS2M 2D flat detector. The data were converted and diffracted intensities integrated using the SNBL software toolbox.[28] Temperature dependent PXRD patterns were plotted and analysed using Powder3D software.[29] Phase composition was verified using the PDF database.[30] Data were fitted using parametric sequential refinements realised in the TOPAS software.[31] The best fits were obtained using a Gaussian peak profile function. Only two crystalline phases, namely $(NH_4)_2[OsCl_6]$ and hcp-Os, were detected in the whole temperature range. Profile parameters for the Gaussian function, cell parameters, and phase fractions were refined simultaneously for both phases.

3. Results and discussion

3.1. X-ray diffraction

Our experiments at low and high temperatures suggest that $(NH_4)_2[OsCl_6]$ does not show any phase transitions below decomposition temperature. Low temperature cooling down to 4 K does not induce any phase changes either. Temperature expansion of cell parameters for $(NH_4)_2[OsCl_6]$ between 293 and 500 K in the form $\alpha(T) = \alpha_0 + \alpha_1 T$ can be fitted using the following exponential approximation:

$$a(T) = a_0 \exp\left[\int_{T_0}^{T} \alpha(T)dT\right] \quad (6)$$

where a_0 is the cell parameter at reference temperature (T_0 = 293 K).[32] The corresponding thermal expansion parameters were determined as follows: a_0 = 9.8662(2) Å (T_0 = 293 K); α_0 = 6.06(7) $\times$ 10^{-5} K^{-1} and α_1 = $-1.7(1) \times 10^{-9}$ K^{-2} (Fig. 1a).

According to the *in situ* PXRD data, visible changes in diffraction patterns can be detected only above 525 K (Fig. 1). TG data show a visible mass loss above 550 K (see ESI,† Fig. S1), which is in agreement with PXRD results. In the whole temperature interval, only starting $(NH_4)_2[OsCl_6]$ and hcp-Os phases can be detected. No visible crystalline intermediates were detected in PXRD profiles. Relative phase fractions characteristic of both phases have been estimated using Rietveld refinement of each diffraction profile. It should be noted that in the intermediate temperature range (525–640 K) diffraction lines characteristic for hcp-Os are relatively broad, which can be associated with the formation of small metallic particles or other amorphous intermediates. The quality of the peak fit and final refinement of the data in the "intermediate" temperature range is degraded because of the increased peak weights due to the presence of poorly crystallized nanoparticles.

The temperature evolution of the estimated phase fractions of $(NH_4)_2[OsCl_6]$ and hcp-Os visually shows a "quasi" two-step

process of thermal decomposition. The first stage (525–640 K) can also be associated with the formation of an amorphous intermediate and relatively small hcp-Os nanoparticles barely seen in the diffraction profiles. Due to the low intensity of relatively broad diffraction lines characteristic of hcp-Os in the first stages of thermal decomposition, information obtained by PXRD on early decomposition stages is strictly limited.

Above 700 K, only the hcp-Os phase can be detected. The refined cell parameters can be used for the calculation of thermal expansion coefficients for a pure Os metal. The corresponding volumetric thermal expansion coefficients were fitted following the analytical dependence of atomic volume on the temperature.[32] The volumetric thermal expansion coefficient in the form

$$\alpha(T) = \alpha_o + \alpha_1 T$$

was obtained by fitting the corresponding dataset to

$$\frac{V(T)}{Z} = \frac{V(T_0)}{Z} \exp\left[\int_{T_0}^{T} \alpha(T)\mathrm{d}T \right] \qquad (7)$$

where $V(T_0)/Z$ is the atomic volume at reference temperature (293 K). The resulting calculated values for α_0 and α_1 together
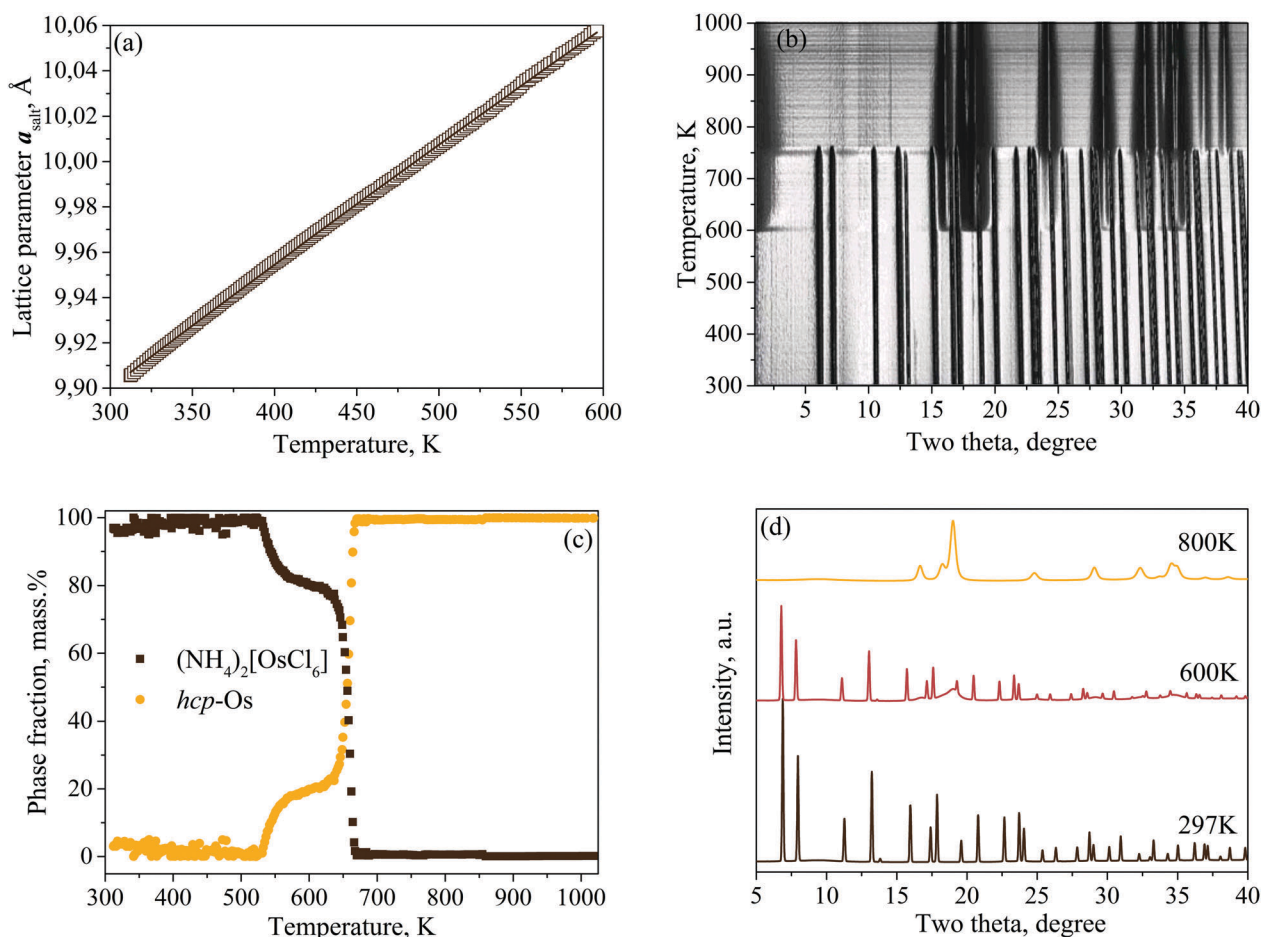

Fig. 1 (a) Temperature dependence of cubic cell parameters on $(NH_4)_2[OsCl_6]$ upon heating (the solid line corresponds to the fitted curves according to eqn (6)); (b) temperature dependence of PXRD patterns (2D-film top view) upon heating the $(NH_4)_2[OsCl_6]$ salt; (c) temperature dependence of weight fractions for $(NH_4)_2[OsCl_6]$ and hcp-Os upon heating refined from PXRD data; (d) selected PXRD patterns obtained at 300, 600 and 800 K. All data were collected in 2 vol% H$_2$/He flow (λ = 0.68894 Å).

33136 | *Phys. Chem. Chem. Phys.*, 2016, **18**, 33134–33141

This journal is © the Owner Societies 2016

Table 1 Volume thermal expansion parameters for hcp-Os upon heating

Composition	V_0/Z, Å^3 atom^{-1} $T = 293.15$ K	$\alpha_0 \times 10^5$ K^{-1}	$\alpha_1 \times 10^8$ K^{-2}	Thermal expansion coefficient at $T = 293$ K, $\alpha(293) \times 10^5$ K^{-1}	Ref.
hcp-Os	13.9843(2)	1.35(1)	0.47(2)	1.36	36
hcp-Os (heating)	13.988(2)	2.73(9)	−1.1(1)	2.7(5)	Present work

with thermal expansion coefficients at 273 K are summarized in Table 1. Thermal expansion of pure hcp-Os has been investigated previously in 1932 and 1976.[33–35]

Arblaster in his recent review[36] summarized that the data for pure Os obtained previously cannot be considered as final due to the limited number of experimental data points reported in the literature and poor agreement between authors.

3.2. X-ray absorption spectroscopy

XANES data can provide a much more detailed information about latent intermediates of the decomposition process. XANES spectra at the Os L$_3$-edge measured during the thermal decomposition of $(NH_4)_2[OsCl_6]$ are presented in Fig. 2a. As the temperature increases up to 574 K a white line originates from the electron transition 2p-unoccupied level and therefore reflects that the density of the unoccupied states shifts to a high-energy range and its intensity decreases. The white line shift is about 0.5 eV as it clearly shows the temperature behaviour of the first order derivative (Fig. 2b). The post-edge peak A originated from a coupling of the final photoelectron state with the localized atomic Cl 3d-states in the structure mediated by multiple scattering deserves special attention.[37] As seen in Fig. 2 and the ESI† Fig. S2, peak A modifies its shape, intensity and position at a temperature that could indicate continuous changes in the first coordination sphere of osmium. The integrated white line area, determined as a difference between the white line area of the spectrum measured at temperatures and that of $(NH_4)_2[OsCl_6]$, decreases in the temperature ranges of 295–440 and 440–525 K demonstrating a different slope in the decrease of the density of the unoccupied states at Os (Fig. 3). This effect results in the positive shift of the absorption edge. A change of the electronic structure can be responsible for an increase of Os charge following the decomposition of $(NH_4)_2[OsCl_6]$ with the formation of low-coordinated intermediates. Taking into account the nature of peak A, the change in its area should correlate with the Os–Cl coordination number in the first Os coordination shell (ESI,† Fig. S2a). However, a difference in the specific area characteristic of peak A for 4 and 6 coordinated Os is not clear. At the same time, osmium halogenides are mainly hexacoordinated independently of the oxidation state.[38]

Fourier transform $k^2\chi(k)$ EXAFS functions in the whole temperature range presented in Fig. 4 demonstrate a temperature-induced behaviour of the pair distribution function of $(NH_4)_2[OsCl_6]$ (here r is an interatomic distance without phase-shift correction and therefore r is lower than the real interatomic distance R). A prominent peak at 1.9 Å in the Fourier transform $k^2\chi(k)$ EXAFS-functions corresponds to the first coordination shell consisting of six chlorine atoms. A monotonic decrease in the amplitude and width of the peak is observed between 320 and 532 K and is
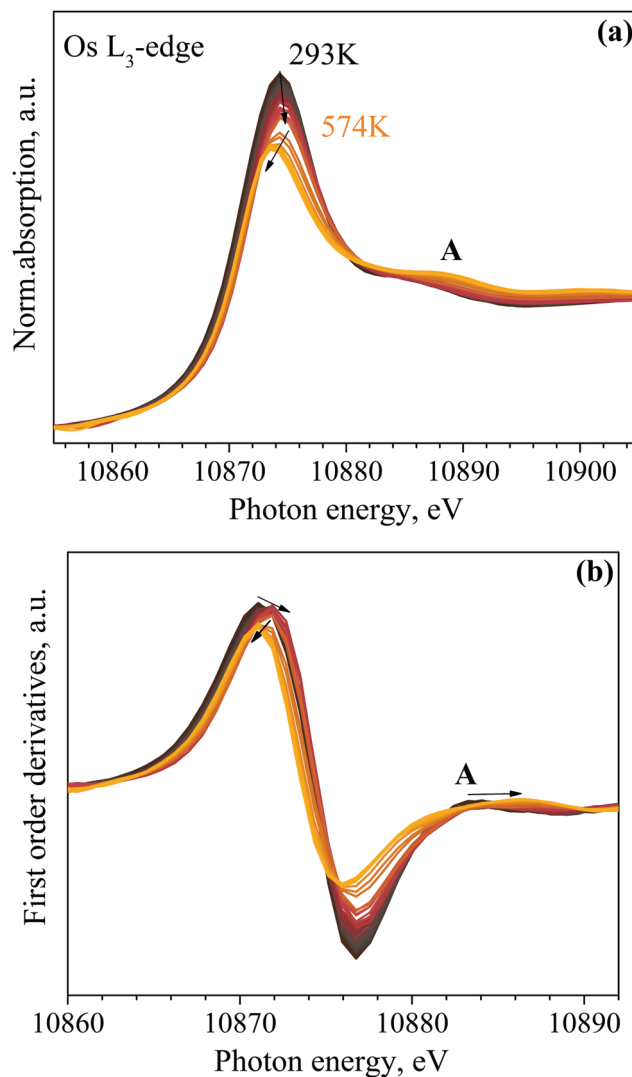

Fig. 2 (a) *In situ* XANES spectra measured in the temperature range of 298–688 K and (b) their first order derivatives.

associated with a thermal disorder and a decrease in the coordination number. Then, the abrupt decrease in the FT is accompanied by a shift in the main Os–Cl peak to a lower distance. Above 574 K, a long-distance shoulder appears at 2.4 Å corresponding to the Os–Os bonds as in metallic Os. With the further increase in temperature, the shoulder amplitude grows to transform into a wide and asymmetric peak at 2.3 Å.

Six chlorine atoms surrounding the absorbing Os atom at a distance of 2.36 Å were taken as an initial single-shell model for refinement of the Os local structure. This model was applied until a contribution of the Os–Os shell originating from
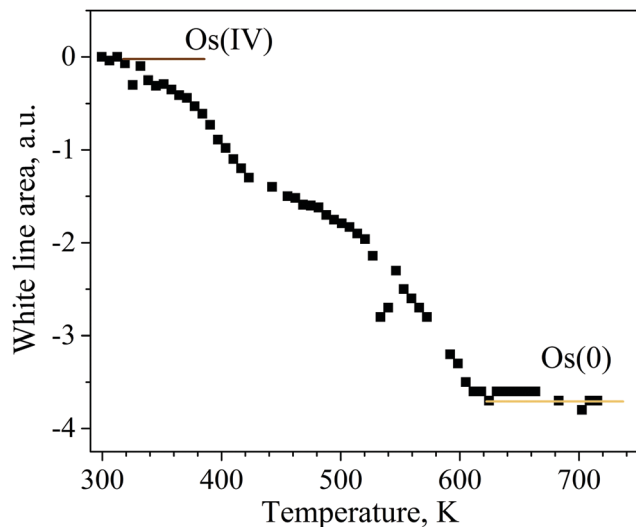
This journal is © the Owner Societies 2016

Phys. Chem. Chem. Phys., 2016, **18**, 33134–33141 | **33137**

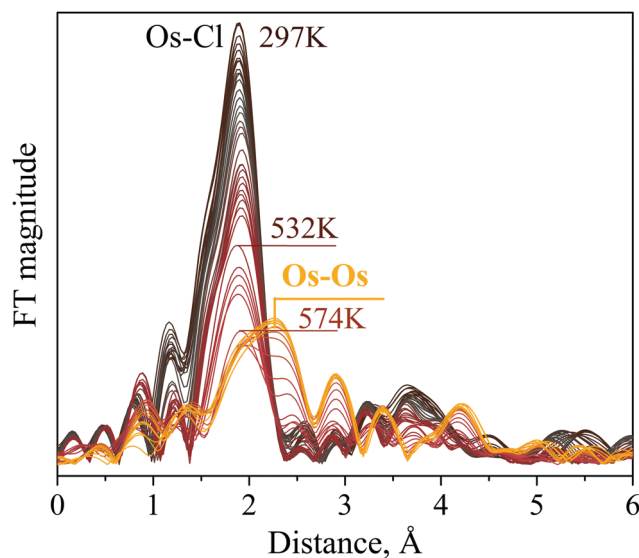**Fig. 3** Difference in the white line area of the XANES spectrum of $(NH_4)_2[OsCl_6]$ and that of measured at temperature.

Fig. 4 Fourier transformed k^2-weighted EXAFS at the Os L_3-edge measured during thermal decomposition of $(NH_4)_2[OsCl_6]$.

Fig. 5 Variation in (a) radius and (b) coordination number of the Os–Cl shell during thermal decomposition of $(NH_4)_2[OsCl_6]$.

metallic Os became prominent. In the least-squares fitting procedure by varying EXAFS parameters such as the interatomic distance (R), the coordination number (N), the Debye–Waller factor (σ^2) and the correction of the threshold energy (ΔE_0), the best parameters were found and are presented in Fig. 5. The spectroscopic factor S_0^2 was determined to be 0.7 for the initial complex at room temperature, when a known coordination number was fixed at 6. Then, the found value of S_0^2 was fixed for all other spectra. At room temperature, the Os–Cl distance was found to be 2.33(1) Å that is in good agreement with 2.36 Å known from XRD.[38] The interatomic distance reaches its maximum 2.36(1) Å at 500 K. Simultaneously, the osmium coordination number, N(Os–Cl), decreases monotonically up to 4 within estimation error. All the revealed changes in the
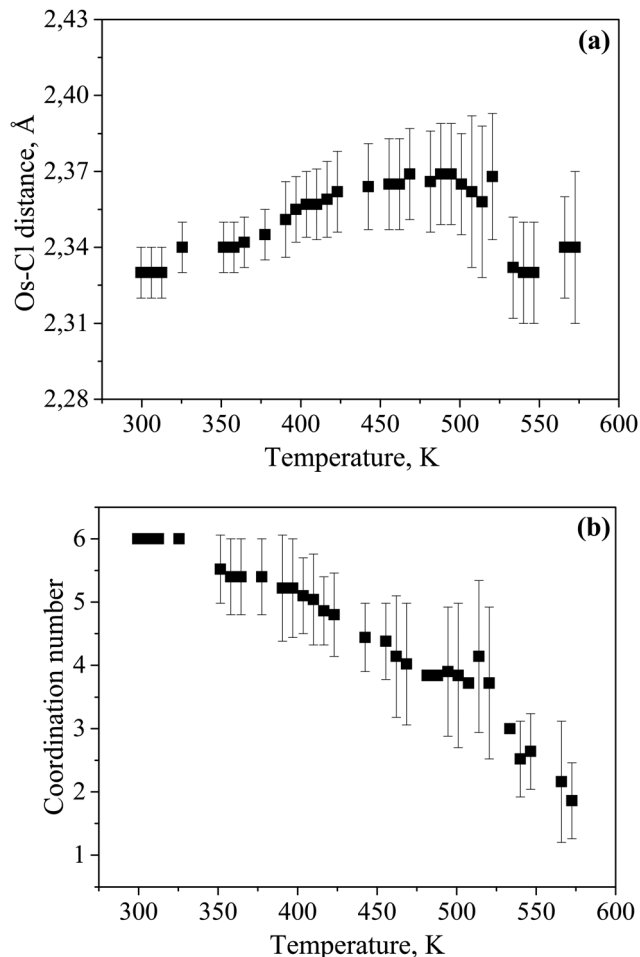
local structure of Os above 500 K present a transformation of octahedrally coordinated Os to a species, where four Cl ions surround Os. Above 525 K, the average Os coordination number continues to decrease to about 2 together with the bond length reaching 2.32(2) Å. Starting from 574 K, the contribution of the metallic Os to EXAFS predominates. Above 600 K, EXAFS spectra are well fitted by pure hcp-Os.

To study the dynamics of $(NH_4)_2[OsCl_6]$, intermediates and the product in the course of the reaction, MCR-ALC analysis has been applied to the experimental XANES and EXAFS data. Only those components containing Os atoms could be detected at the Os L_3-edge and molecules such as HCl, NH_3 or NH_4Cl were not included in the analysis. The XANES and EXAFS spectra of three statistically meaningful components were selected (Fig. 6.) The concentrations of other components were too low (less than 5%) to be included in further analysis due to their proximity to the error bar of the signal-to-noise ratio of the data. As the optimum lack of the fit of the experimental data matrix was 4%, the percentage of variance explained was 99.83%. The results of the MCR-ALS analysis with an inclusion of the selected components corresponding to the starting $(NH_4)_2[OsCl_6]$, one intermediate compound and metallic osmium are presented in Fig. 7.

Fig. 7 The temperature-induced behaviour of the $(NH_4)_2[OsCl_6]$ reactant and the component formed in the course of its thermal decomposition obtained by MCR-ALS analysis.
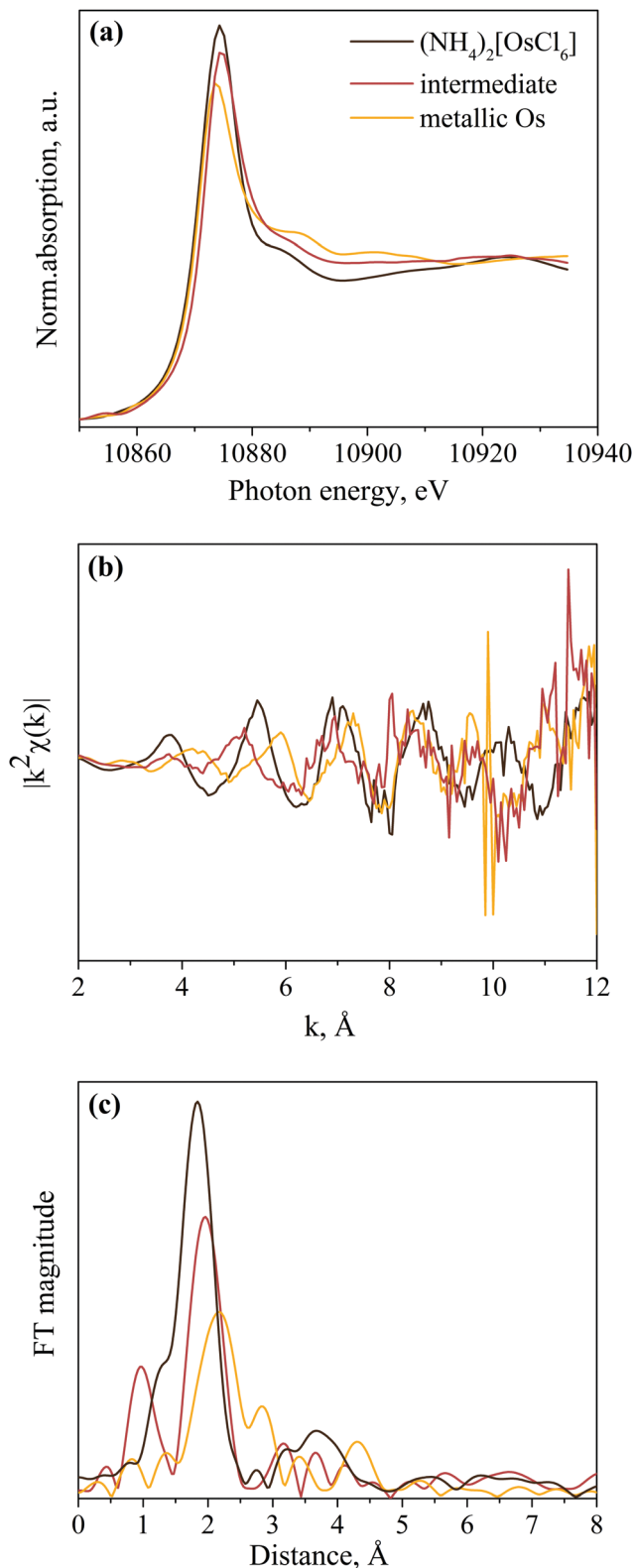

Fig. 6 (a) XANES, (b) EXAFS and (c) Fourier transformed k^2-weighted EXAFS of the components selected by MCR-ALS.

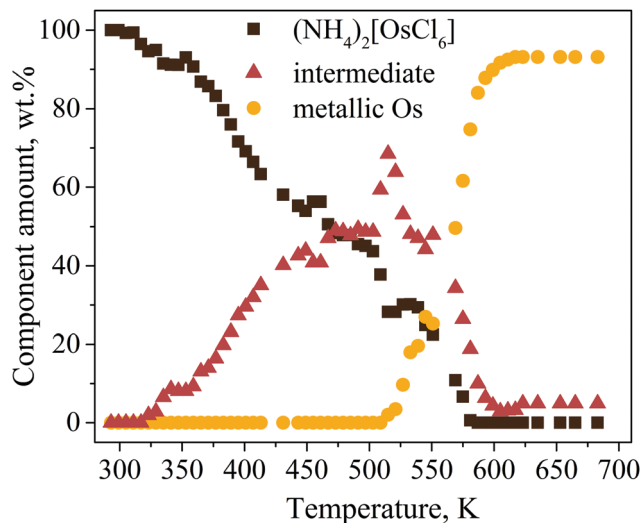The intermediate compound is formed above 320 K and its amount grows with temperature reaching the maximum at 525 K. Only above 525 K, a visible amount of metallic Os can be detected. Thus, the decrease in the white line area below 525 K should be associated only with a change in the electronic structure of Os in the intermediate species. The following relatively fast decrease in the white line area (Fig. 3) comes from an averaging of the Os oxidation state over Os(IV) and Os(0). The behaviour of the metallic and the intermediate components clearly shows that a two-step chemical reaction occurred under thermal decomposition.

As XAFS describes the average over all possible local atomic and electronic structures around the absorbing atom in the sample, the selected XANES (Fig. 6a) and EXAFS (Fig. 6b) by MCR-ALS allow the local atomic structure of Os to be disclosed in the intermediate compound. The Fourier transform of selected EXAFS-functions were obtained under similar conditions to all other experimental data (Fig. 6c). A decrease in the FT magnitude of the intermediate is seen to be about 40% with respect to that of the initial complex compound. The FT of this intermediate compound (Fig. 6c) is comparable with that presented in Fig. 4 at about 500 K. Unfortunately, EXAFS fitting of the intermediate does not provide very precise results because of the noise of the selected EXAFS-oscillations in the high k range (Fig. 6b). Nevertheless, the Os–Cl bond length and the coordination number were estimated to be 2.37(2) Å and 4.0(4), respectively. (Quality of the fitting is evaluated in the ESI,† Fig. S3.) Similar EXAFS parameters were observed in the temperature range of 480–525 K (Fig. 5a and b) indicating that the intermediate compound predominates at these temperatures. This agrees well with the results presented in Fig. 7. As the intermediate was not detected by PXRD a polymer nature of the intermediate could be suggested.

Summarizing the analysis presented above, both techniques, *in situ* PXRD and XAFS, provide direct evidence of the two-stage nature of $(NH_4)_2[OsCl_6]$ decomposition. It is worth noting that the first stage occurs at different temperatures in XANES and PXRD. The plateau in the temperature-dependent weight

fractions for crystalline phases obtained by PXRD (Fig. 1c) can be directly attributed to the predominant formation of the intermediate species detected by XAFS (Fig. 7). PXRD and XAFS experiments were carried out at the different beamlines and different apparatuses with own specifics, so the temperature-induced reaction could be shifted in time and therefore in temperature. As information on the amorphous intermediate is very limited in PXRD, the phase ratio for crystalline phases does not show complete Os balance during the reaction. Nevertheless, temperature behaviours of phase fractions detected by XRD (Fig. 1) and the Os white line detected by XAFS (Fig. 3) show similar trends. Namely, both techniques show a plateau (100 K length) where phase fractions and the Os oxidation state do not vary. Above 640 K (Fig. 1) the fraction corresponds to the rapid growth of the hcp-Os phase predominately at the expense of the reduction of the intermediate. Thus, the first stage concerns the formation of the Os-containing intermediate species. The intermediate is formed above 325 K. At 525 K, its amount reaches about 60% and at the same time the component characteristic of hcp-Os appears.

4. Conclusions

Previous investigations under non-isothermal conditions in a reducing atmosphere based on thermogravimetric analysis and *ex situ* investigations suggested the one-step decomposition of $(NH_4)_2[OsCl_6]$ according to the following reaction:

$$3(NH_4)_2[OsCl_6] \rightarrow 3Os + 2N_2 + 16HCl + 2NH_4Cl.$$
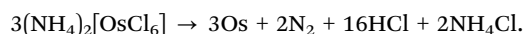
The reaction investigated using time-resolved energy-dispersive XAFS and *in situ* PXRD appears to be more complex. At least one amorphous species with a polymer structure and four-coordinated Os can be suggested to be the main intermediate.

XAFS analysis shows that the thermal decomposition of $(NH_4)_2[OsCl_6]$ starts with the formation of the intermediate $\{OsCl_4\}_x$ species, which reaches its maximum at 525 K, and then the metallic Os appears. Further mass-loss can be associated with the decomposition of the $\{OsCl_4\}_x$ intermediate:

$$(NH_4)_2[OsCl_6] \rightarrow \{OsCl_4\}_x + NH_4Cl$$

$$\{OsCl_4\}_x \rightarrow Os \tag{8}$$
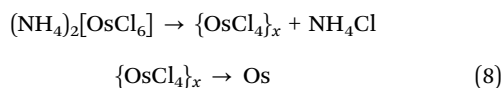
First a small amount of metallic Os can be detected at about 500 K by XAFS. Direct decomposition of $(NH_4)_2[OsCl_6]$ in H_2 flow with the formation of $\{OsCl_4\}_x$ and NH_4Cl occurs on the surface of the sample as a parallel reaction. A plateau detected by XAFS and PXRD can be associated with several factors. Mainly thermally controlled growth of nano-dimensional hcp-Os particles and a blockade of the reactant by Os and NH_4Cl products should control the reaction kinetics. The temperature increase leads to sublimation of NH_4Cl and the growth of Os particles.

A visually simple reaction proposed to be elementary can show a complex nature upon investigation using complementary powerful techniques. We suspect that thermal decomposition of other hexahalogenometallates such as $(NH_4)_2[IrCl_6]$ and $(NH_4)_2[ReCl_6]$ being studied by modern physicochemical methods may show complex thermal decomposition behaviour. Detailed knowledge on the mechanism for their thermal decomposition will lead to a better understanding of the solid-state reactivity and stability of many coordination compounds especially species important as intermediates and pharmaceutical active ingredients.

Notes and references

1 F. Wöhler, *Lehrbuch der Chemie Bd.2*, 951, Dresden, 1826.
2 P. Vallet, *C. R. Acad. Sci.*, 1932, **195**, 1075.
3 I. Alonso-Lemus, Y. Verde-Gomez and L. Alvarez-Contreras, *Int. J. Electrochem. Sci.*, 2011, **6**, 4176.
4 *Microwave Heating as a tool for sustainable chemistry*, ed. N. E. Leadbeater, CRC Press Taylor@Francis Group, 2010, ch. 6.
5 T. T. Cheng and E. L. Gyenge, *J. Appl. Electrochem.*, 2008, **38**, 51.
6 R. Frahm, *Nucl. Instrum. Methods Phys. Res., Sect. A*, 1988, **270**, 578.
7 R. Frahm, *Rev. Sci. Instrum.*, 1989, **60**, 2515.
8 T. Nonaka, K. Dohmae, T. Araki, Y. Hayashi, Y. Hirose, T. Uruga, H. Yamazaki, T. Mochizuki, H. Tanida and S. Goto, *Rev. Sci. Instrum.*, 2012, **83**, 083112.
9 Q. Kong, F. Baudelet, J. Han, S. Chagnot, L. Barthe, J. Headspith, R. Goldsbrough, F. E. Picca and O. Spalla, *Sci. Rep.*, 2012, **2**, 1018.
10 O. Müller, M. Nachtegaal, J. Just, D. Lützenkirchen-Hechta and R. Frahma, *J. Synchrotron Radiat.*, 2016, **23**, 260.
11 G. Meyer and A. Möller, *J. Less-Common Met.*, 1991, **170**, 327.
12 H. Rumpf, H. Modrow, J. Hormes, P. Amann, A. Möller and G. Meyer, *J. Synchrotron Radiat.*, 2001, **8**, 707.
13 H. Rumpf, J. Hormes, A. Möller and G. Meyer, *J. Synchrotron Radiat.*, 1999, **6**, 468.
14 P. Norby, R. Dinnebier and A. N. Fitch, *Inorg. Chem.*, 2002, **41**, 3628.
15 S. G. Fiddy, M. A. Newton, A. J. Dent, G. Salvini, J. M. Corker, S. Turin, T. Campbell and J. Evans, *Chem. Commun.*, 1999, 851.
16 S. Pascarelli and O. Mathon, *Phys. Chem. Chem. Phys.*, 2010, **12**, 5535.
17 R. I. Walton, A. J. Dent and S. J. Hibble, *Chem. Mater.*, 1998, **10**, 3737.

33140 | *Phys. Chem. Chem. Phys.*, 2016, **18**, 33134–33141

This journal is © the Owner Societies 2016

18 P. Zalden, G. Aquilanti, C. Prestipino, O. Mathon, B. André, M. Wuttig and M. V. Coulet, *J. Synchrotron Radiat.*, 2012, **19**, 806.

19 R. Kodama, Y. Terada, I. Nakai, S. Komaba and N. Kumagai, *J. Electrochem. Soc.*, 2006, **153**, A583.

20 J. M. Thomas and G. N. Greaves, *Catal. Lett.*, 1993, **20**, 337.

21 S. Pascarelli, O. Mathon, T. Mairs, I. Kantor, G. Agostini, C. Strohm, S. Pasternak, F. Perrin, G. Berruyer, P. Chappelet, C. Clavel and M. C. Dominguez, *J. Synchrotron Radiat.*, 2016, **23**, 353.

22 I. Kantor, J.-C. Labiche, E. Collet, L. Siron, J.-J. Thevenin, C. Ponchut, J. Borrel, T. Mairs, C. Marini, C. Strohm, O. Mathon and S. Pascarelli, *J. Synchrotron Radiat.*, 2014, **21**, 1240.

23 B. Ravel and M. Newville, *J. Synchrotron Radiat.*, 2005, **12**, 537.

24 M. Newville, *J. Synchrotron Radiat.*, 2001, **8**, 322.

25 J. Jaumot, R. Gargallo, A. de Juan and R. Tauler, *Chemom. Intell. Lab. Syst.*, 2005, **76**, 101.

26 J. Jaumot, A. de Juan and R. Tauler, *Chemom. Intell. Lab. Syst.*, 2015, **140**, 1.

27 T. Asanova, I. Asanov, A. Zadesentz, E. Filatov, P. Plusnin, E. Gerasimov and S. Korenev, *J. Therm. Anal. Calorim.*, 2016, **123**, 1183.

28 V. Dyadkin, *SNBL Tool box*, Swiss Norwegian Beamline at ESRF, Grenoble, France, 2013.

29 P. Rajiv, R. Dinnebier and M. Jansen, *Mater. Sci. Forum*, 2010, **651**, 97.

30 PDF-2 Release 2012 (Database), ed. S. Kabekkodu, International Centre for Diffraction Data, Newtown Square, PA, USA, 2012.

31 *TOPAS v.4.0*, Bruker AXS, Bruker-AXS 5465 East Cheryl Parkway, 2009.

32 R. S. Krishnan, R. Srinavasan and S. Devanarayanan, *International series on the science of the solid state*, Pergamon Press, Oxford, 1979, vol. 22.

33 E. A. Owen and E. W. Roberts, *Philos. Mag.*, 1936, **22**, 290.

34 E. A. Owen and E. W. Roberts, *Z. Kristallogr.*, 1937, **A96**, 497.

35 R. H. Schröder, N. Schmitz-Pranghe and R. Kohlhaas, *Z. Metallkd.*, 1972, **63**, 12.

36 J. W. Arblaster, *Platinum Met. Rev.*, 2013, **57**, 177.

37 A. L. Ankudinov, J. J. Rehr and S. R. Bare, *Chem. Phys. Lett.*, 2000, **316**, 495.

38 S. A. Cotton, *Chemistry of precious metals*, Uppingham School, Rutland, UK, 1997.